



저작자표시-비영리-변경금지 2.0 대한민국

이용자는 아래의 조건을 따르는 경우에 한하여 자유롭게

- 이 저작물을 복제, 배포, 전송, 전시, 공연 및 방송할 수 있습니다.

다음과 같은 조건을 따라야 합니다:



저작자표시. 귀하는 원저작자를 표시하여야 합니다.



비영리. 귀하는 이 저작물을 영리 목적으로 이용할 수 없습니다.



변경금지. 귀하는 이 저작물을 개작, 변형 또는 가공할 수 없습니다.

- 귀하는, 이 저작물의 재이용이나 배포의 경우, 이 저작물에 적용된 이용허락조건을 명확하게 나타내어야 합니다.
- 저작권자로부터 별도의 허가를 받으면 이러한 조건들은 적용되지 않습니다.

저작권법에 따른 이용자의 권리는 위의 내용에 의하여 영향을 받지 않습니다.

이것은 [이용허락규약\(Legal Code\)](#)을 이해하기 쉽게 요약한 것입니다.

[Disclaimer](#)

M.S. Thesis

# Interface Design of Hyperbolic Metamaterials for Tunable Scattering

제어 가능한 산란 특성을 위한 쌍곡선형  
메타물질에서의 계면 설계

BY

Jiho Hong

February 2016

DEPARTMENT OF ELECTRICAL AND COMPUTER  
ENGINEERING  
COLLEGE OF ENGINEERING  
SEOUL NATIONAL UNIVERSITY

# Abstract

An interface between media plays a critical role in controlling the flow of elementary particles, by introducing the violated continuity of particle flows. In optics, the efficient change of wavevectors through interfaces has been the foundation of optical elements, such as mirrors, lens, and waveguides.

Overcoming the previous belief that the interface should be composed between ‘different’ media, the recently proposal of ‘metasurfaces’ which can be made in-between identical materials generates strong scattering of waves through the discontinuity in amplitude and phase across the surfaces. However, in spite of their name of meta-‘surface’, they are composed of elements with ‘finite’ thickness to increase the scattering. The benefits of a single interface have thus not been fully exploited in existing metasurfaces.

In this thesis, we investigate an artificial interface between identical metamaterials. From both analytic and numerical analysis, we verify that a dislocated interface between identical hyperbolic metamaterials can provide the full range of transmission phase shift with unity transmittance, including the regime of ‘phase reversal’. By exploiting the advantages of ‘zero-thickness’ phase control, various platforms based on the dislocated interfaces are proposed for applications on controlling wave propagation in hyperbolic metamaterials.

**Keywords:** Metasurface, Hyperbolic metamaterial, Dislocation

**Student Number:** 2014-21710

# Table of Contents

<b>Abstract</b> .....	<b>i</b>
<b>Table of Contents</b> .....	<b>ii</b>
<b>List of Figures</b> .....	<b>iv</b>
<b>Chapter 1 Introduction</b> .....	<b>1</b>
<b>1.1 Background of research</b> .....	<b>1</b>
<b>1.2 Objective</b> .....	<b>5</b>
<b>1.3 Outline of the thesis</b> .....	<b>7</b>
<b>Chapter 2 Hyperbolic metamaterials</b> .....	<b>8</b>
<b>2.1 Hyperbolic dispersion relation</b> .....	<b>9</b>
<b>2.2 Numerical methods</b> .....	<b>1 2</b>
<b>2.2.1 Correct factorization rule</b> .....	<b>1 3</b>
<b>2.2.2 Adaptive spatial resolution</b> .....	<b>1 4</b>
<b>2.3 Fabrication</b> .....	<b>1 5</b>
<b>Chapter 3 Interface between HMMs</b> .....	<b>1 9</b>

3.1	Boundary conditions for a single interface...	2 0
3.2	Dislocated interface between HMMs.....	2 2
3.3	High- $k$ and low- $k$ mode transitions .....	2 7
3.4	Engineering of isofrequency contours.....	2 9
<b>Chapter 4 Conclusion .....</b>		<b>3 2</b>
<b>Bibliography .....</b>		<b>3 4</b>
<b>Abstract in Korean.....</b>		<b>3 6</b>

# List of Figures

Figure 1.1 Electromagnetic material parameter space characterized by permittivity ( $\epsilon$ ) and permeability ( $\mu$ ) [1].....	2
Figure 1.2 (a)-(b) Examples of electromagnetic metamaterials: (a) double-negative index [2] and (b) high refractive index metamaterials [3]. (c) Metamaterial structures and electric field distributions for electromagnetic cloaking [8].....	3
Figure 1.3 Examples of metasurface structures: (a) anomalous refraction [9], (b) anomalous reflection [10], (c) optical vortex [9], and (d) ultrathin Fabry-Perot resonator [12]. .....	4
Figure 1.4 Finite-thickness structures of the previously proposed metasurfaces: (a, c) multilayered structures for transmission-type metasurfaces [11, 13], (b) magnetic metasurface [14], and (d) metasurface absorber [15].....	6
Figure 2.1. (a)-(b) Isofrequency surfaces of indefinite effective permittivity tensors: (a) $\epsilon_{\perp}>0$ and $\epsilon_{\parallel}<0$ , (b) $\epsilon_{\perp}<0$ and $\epsilon_{\parallel}>0$ . (c)-(d) Example structures of HMMs: (c) metallic wire arrays and (d) metal-dielectric layered structure [16]. .....	9
Figure 2.2. (a)-(b) Equivalent capacitor model for (a) $\epsilon_{\parallel}$ and (b) $\epsilon_{\perp}$ . (c) IFCs from EMA (solid line) and the Fourier modal method (circle)....	1 1
Figure 2.3. Applications of HMMs: (a) hyperlens for imaging below diffraction limit [19], (b) enhanced Purcell effect for quantum dots [22], (c) broadband absorber [21], and (d) subwavelength resonator	

with anomalous scaling laws [20].	1 2
Figure 2.4. Example results of Fourier factorizations based on the Laurent's rule (oscillatory line) and IR (nonoscillatory line) [24].	1 4
Figure 2.5. Examples of ASR: (a) finite Fourier series in different coordinate systems, and (b) adaptive coordinates for a single split-ring resonator [23].	1 5
Figure 2.6. Fabrication examples of HMMs: (a) metal-dielectric multilayer [25], (b) spherical hyperlens [26], (c) optical resonator [20], and (d) broadband absorber [27].	1 6
Figure 2.7. Fabrication process of the metal-dielectric layered HMM with one-dimensionally periodic modulation.	1 7
Figure 2.8. SEM images of the fabricated HMM at (a) cross-section view and (b) tilted view.	1 8
Figure 3.1. According to Eqs. (3.3) and (3.4) for the TM-incidence, (a) reflectance, (b) transmittance, (c) reflection phase and (d) transmission phase as a function of two parameters, $\theta$ and $\varphi$ .	2 2
Figure 3.2. (a) Schematics of the dislocated HMMs with dislocation $\Delta$ , and the metasurface model between identical homogeneous media with an effective permittivity tensor $\epsilon_{\text{eff}}$ . (b) $ \mathbf{E} $ distributions and $\mathbf{E}$ -field vectors, and (c) $H_z$ distributions and $\mathbf{D}$ -field vectors for the singular reflection point ( $d=\lambda/100$ ).	2 3
Figure 3.3. (a) Reflectance, (b) transmittance, (c) reflection phase and (e) transmission phase under the fundamental mode incidence from the bulk HMM as a function of dislocation $\Delta$ and tangential wavevector $k_y/k_0$ ( $d=\lambda/100$ ).	2 5
Figure 3.4. Magnetic field distributions ( $H_z$ ) for the specific cases: (a) perfect reflection and (b) perfect transmission for the normal incidence $k_y/k_0=0$ , and (c) phase-maintained and (d) phase-reversed perfect transmission for the oblique incidences $k_y/k_0=\pm 5$ ( $d=\lambda/100$ ).	2 6
Figure 3.5. (a) Schematic of the generalized Snell's law with a phase gradient [9]. (b) Different values of $\Delta$ which are chosen for forming a linear	

phase gradient in steps of $\pi/8$ .....	2 7
Figure 3.6. The magnetic field distributions ( $H_z$ ) for (a) high- $k$ and (b) low- $k$ mode transitions with the values of $\Delta$ which are chosen in Fig. 3.5b. Insets in (a) and (b) show the schematics of the unit cell structure for local transmission phase. ....	2 9
Figure 3.7. The modulated IFCs of HMM (a) as a function of $\Delta$ and (b) for the specific sizes of the dislocation ( $\Delta/d=0.35, 0.45, 0.55, 0.65$ ). The inset in (a) shows the schematic of the periodic array of alternating dislocated interfaces with dislocation $\Delta$ and period $L_x$ . (b) The full-wave numerical analysis based on the finite element method confirms the validity of the results from TMM.....	3 1

# Chapter 1

## Introduction

### 1.1 Background of research

Metamaterials are artificially designed materials which have properties that are not found in nature. In general, conventional materials consisting of atoms and molecules are considered as homogenous media in the macroscopic viewpoint. Similarly, composite structures of subwavelength inclusions, called meta-atoms, could be described as effective homogenous media. Since their effective material properties are determined from geometric shape and arrangement of meta-atoms, it could be possible to obtain desired material properties by carefully designing metamaterial structures in the subwavelength regime.

In electromagnetics and optics, electric and magnetic properties of materials are characterized by macroscopic permittivity and permeability (Fig. 1.1 [1]). Thus, there has been efforts to realize metamaterials of extreme permittivity and

permeability, such as double negative (Fig. 1.2a) [2], high refractive index (Fig. 1.2b) [3], and zero-index metamaterials [4]. Furthermore, since the local effective material properties could be manipulated by adjusting the structural parameters of each meta-atom, it could be possible to obtain desired spatial distributions of material properties. Combining with theoretical approaches for controlling wave propagation, such as transformation optics [5], conformal optics [6] and optical circuit [7], metamaterials have been employed for manipulation of wave propagation, for example, electromagnetic cloaking (Fig. 1.2c) [8].

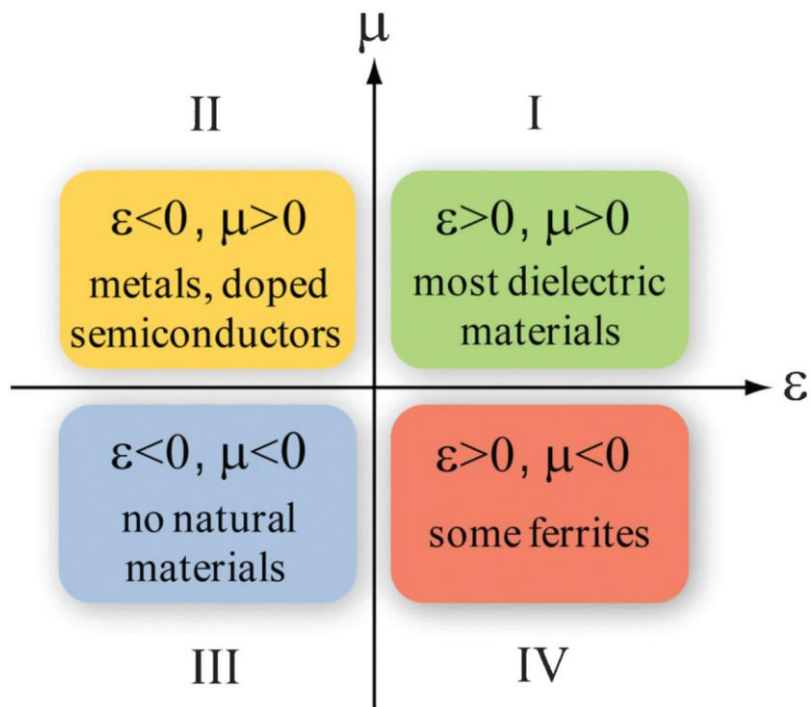


Figure 1.1 Electromagnetic material parameter space characterized by permittivity ( $\epsilon$ ) and permeability ( $\mu$ ) [1].

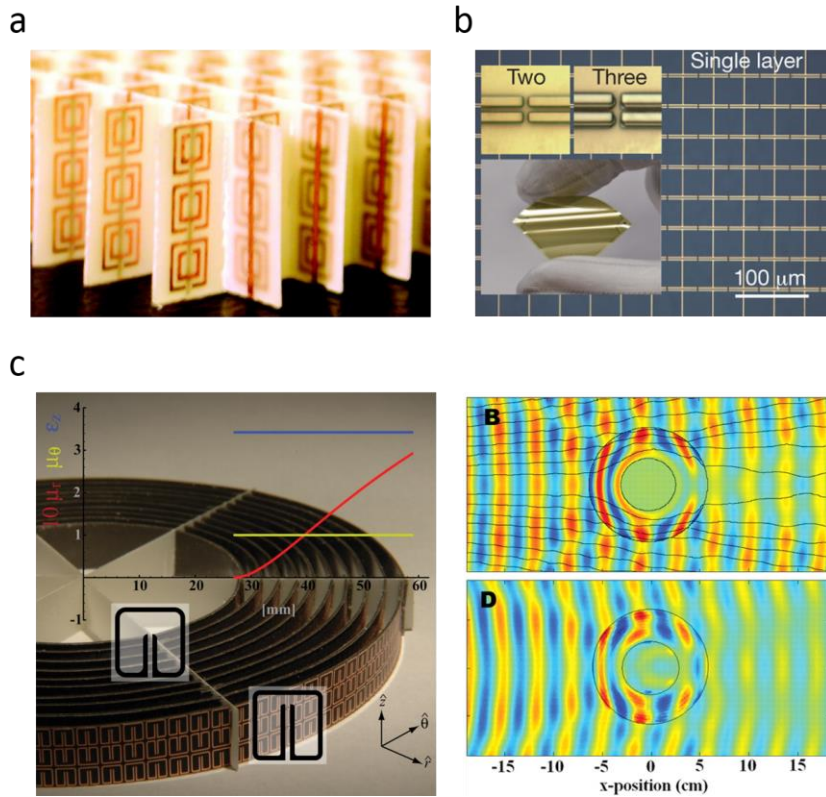


Figure 1.2 (a)-(b) Examples of electromagnetic metamaterials: (a) double-negative index [2] and (b) high refractive index metamaterials [3]. (c) Metamaterial structures and electric field distributions for electromagnetic cloaking [8].

Recently, the concept of metasurfaces was proposed [9]. Metasurfaces are low-dimensional metamaterials to impose phase and amplitude discontinuities across the surfaces. In contrast to the three-dimensional metamaterials, metasurfaces could be fabricated with relative ease by virtue of their planar geometry. Utilizing a wide range of phase shift depending on the structural parameters of metasurfaces, desired wavefront of transmitted (or reflected) waves could be obtained by tuning the local phase shifts in transmission (or reflection).

When metasurfaces offer a linear phase gradient, incident waves could be anomalously refracted or reflected at the surface (Figs. 1.3a and 1.3b) [9, 10]. Since these phase shifts occur within the subwavelength thickness, metasurfaces allow the reduction of device dimensions into the subwavelength regime, and thus could realize ultrathin devices, such as ultrathin optical lens [11] and resonators [12].

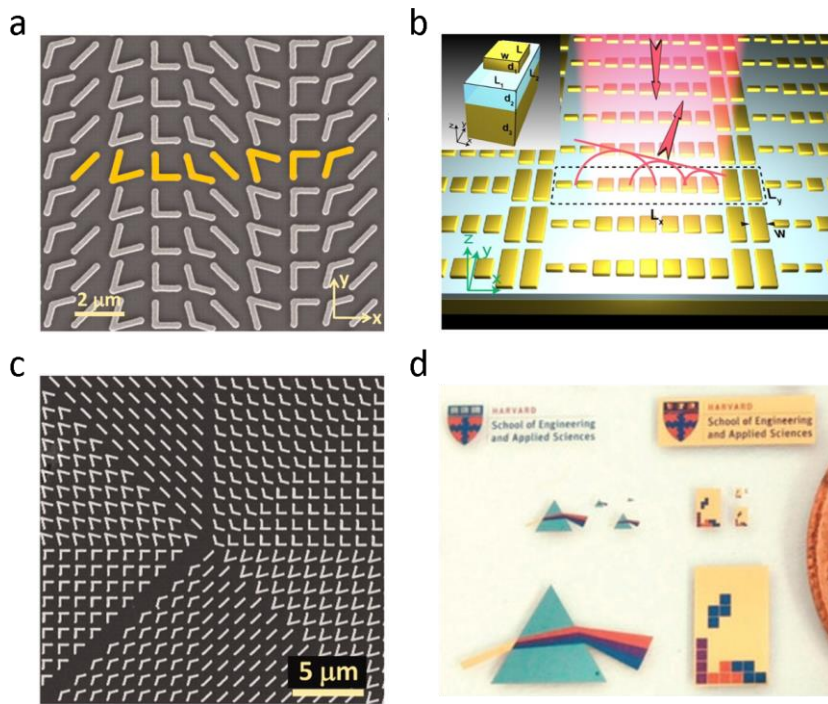


Figure 1.3 Examples of metasurface structures: (a) anomalous refraction [9], (b) anomalous reflection [10], (c) optical vortex [9], and (d) ultrathin Fabry-Perot resonator [12].

## 1.2 Objective

It had been widely believed that the scattering of waves could be achieved only at the interface between ‘different’ media. Such a belief has been broken by the recently proposal of ‘metasurfaces’ [9]. By providing amplitude and phase discontinuities across the interface, metasurfaces could even generate the scattering between identical media. Although the previously proposed metasurfaces have been called a ‘surface’, they have finite thickness to enhance the scattering efficiencies (Fig. 1.4) [11, 13-15]. In transmission-type metasurfaces, for instance, multilayered structures have been employed for high-efficiency optical devices (Fig. 1.4a) [11]. As a result, the benefits of a single interface have not been fully exploited in the previous platforms of metasurfaces, which enable novel applications, such as a zero-thickness phase device.

Promising candidates for a single-interface metasurface are interfaces between metamaterials. Although there has been much efforts on investigating the interface physics and applications, they have focused only on natural or artificial interfaces between natural media, neglecting the possibility of artificial interfaces between ‘artificial’ media. Especially, in contrast to negligible interfaces between identical natural media, interfaces between identical metamaterials could have the potential to generate strong interface scattering. In the subwavelength regime, these interfaces could be considered as a single surface in homogenous effective media, allowing optical functionalities even with zero thickness.

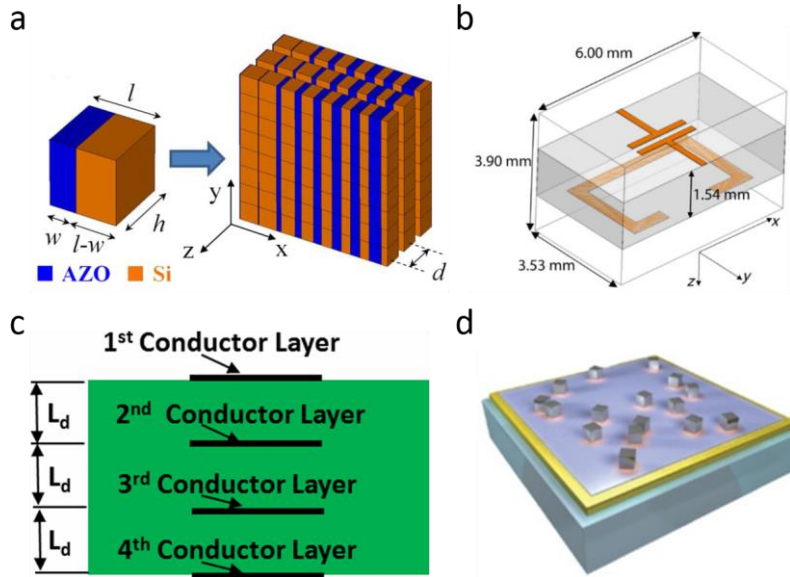


Figure 1.4 Finite-thickness structures of the previously proposed metasurfaces: (a, c) multilayered structures for transmission-type metasurfaces [11, 13], (b) magnetic metasurface [14], and (d) metasurface absorber [15].

In this thesis, we investigate an artificial interface between artificial media. We demonstrate that an interface between identical metamaterials could provide drastic amplitude and phase discontinuities across the single surface, namely a zero-thickness metasurface. Considering hyperbolic metamaterials (HMMs) in the form of alternating metallic and dielectric layers, it is shown that under an oblique incidence, a dislocated interface between identical HMMs can provide the full range of transmission phase shift with unity transmittance, including the regime of ‘phase reversal’. By exploiting the advantages of ‘zero-thickness’ phase control, various platforms based on the dislocated interfaces are proposed for applications on controlling wave propagation in HMMs.

### 1.3 Outline of the thesis

In chapter 2, we briefly review the fundamentals and applications of HMMs, including numerical methods and fabrication process for HMMs. In chapter 3, we first derive an analytic model of single-interface scattering between identical media, and numerically investigate a dislocated interface in the metal-dielectric layered HMM. From these analytic and numerical analysis, we verify that the dislocated interface allows optical functionalities even with zero-thickness metasurface, creating novel phenomena, such as phase-reversed transmission and topological phase transitions. Based on the scattering properties of the dislocated interface, we also propose several platforms for applications on controlling wave propagation in HMMs: high- $k$  and low- $k$  mode transitions, and engineering of isofrequency contours (IFCs).

## Chapter 2

# Hyperbolic metamaterials

Hyperbolic metamaterials (HMMs) are extremely anisotropic media which are described by indefinite effective permittivity tensors. Since the principal values of the effective permittivity tensors have opposite signs, the isofrequency contour (IFC) of HMMs is hyperbolic for extraordinary waves. In contrast to elliptic materials, the indefinite IFC allows large-wavevector propagating waves and high photonic density of states. Under the effective medium approximation (EMA), HMMs are usually realized as two-dimensional composites of metals and dielectrics, for instance, metal-dielectric layered structures (Fig. 2.1d), and metallic wire arrays in dielectric host (Fig. 2.1c). Especially, the metal-dielectric layered HMMs have attracted much attention because of their simple fabrication process. In this chapter, we briefly review the fundamentals and applications of HMMs, focusing on the form of alternating metallic and dielectric layers.

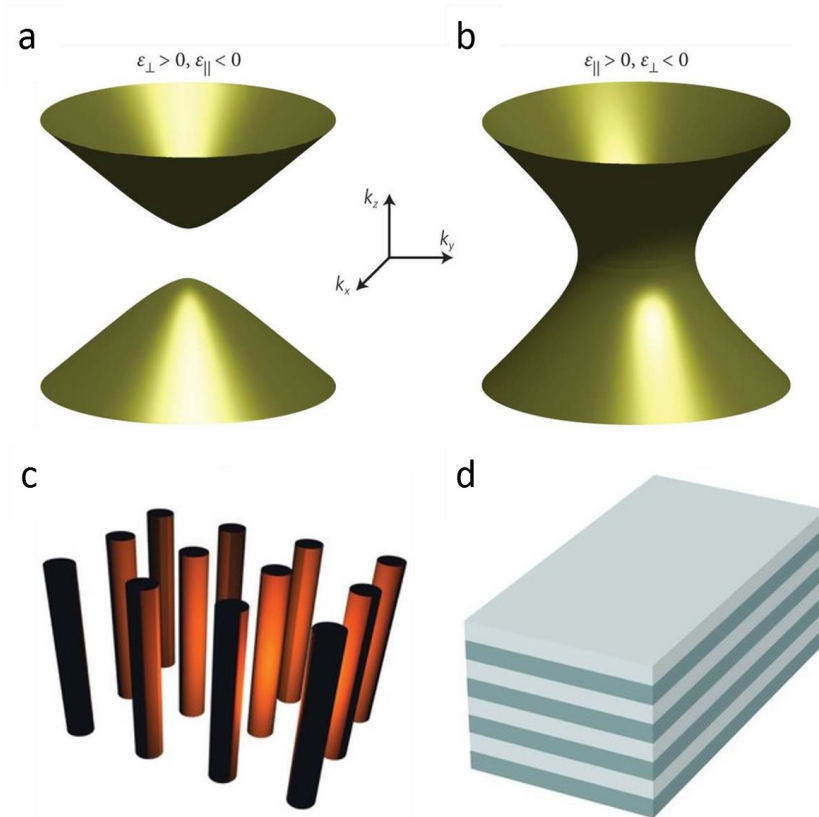


Figure 2.1. (a)-(b) Isofrequency surfaces of indefinite effective permittivity tensors: (a)  $\epsilon_{\perp} > 0$  and  $\epsilon_{\parallel} < 0$ , (b)  $\epsilon_{\perp} < 0$  and  $\epsilon_{\parallel} > 0$ . (c)-(d) Example structures of HMMs: (c) metallic wire arrays and (d) metal-dielectric layered structure [16].

## 2.1 Hyperbolic dispersion relation

In the subwavelength regime, the physics of HMMs is described by EMA which provides effective permittivity tensors. For the metal-dielectric layered structures, the effective anisotropic material parameters are given as follows:

$$\varepsilon_{\parallel} = (1-f)\varepsilon_d + f\varepsilon_m \quad (2.1)$$

$$\varepsilon_{\perp} = \frac{\varepsilon_d \varepsilon_m}{(1-f)\varepsilon_m + f\varepsilon_d} \quad (2.2)$$

where  $\varepsilon_d$  and  $\varepsilon_m$  are the relative permittivities of a dielectric and a metal respectively, and  $f$  is the filling factor of a metal. Under the quasi-static assumption, these effective material parameters,  $\varepsilon_{\parallel}$  and  $\varepsilon_{\perp}$ , are corresponding to the equivalent capacitance for parallel (Fig. 2.2a) and series (Fig. 2.2b) combinations, respectively. In the case of the metallic wire arrays in dielectric host, the effective anisotropic material parameters are also given by [17]

$$\varepsilon_{\parallel} = \frac{(1+f)\varepsilon_d \varepsilon_m + (1-f)\varepsilon_d^2}{(1-f)\varepsilon_m + (1+f)\varepsilon_d} \quad (2.3)$$

$$\varepsilon_{\perp} = (1-f)\varepsilon_d + f\varepsilon_m \quad (2.4)$$

Since a metal and a dielectric have opposite electric properties ( $\varepsilon_m < 0$  and  $\varepsilon_d > 0$ ), the effective permittivity tensor of the multilayered structures should be indefinite ( $\varepsilon_{\perp} \varepsilon_{\parallel} < 0$ ). Therefore, the metal-dielectric layered structures have hyperbolic dispersion for extraordinary waves (Fig. 2.2c).

$$\frac{k_{\perp}^2}{\varepsilon_{\parallel}} + \frac{k_{\parallel}^2}{\varepsilon_{\perp}} = k_0^2 \quad (\varepsilon_{\parallel} \varepsilon_{\perp} < 0) \quad (2.5)$$

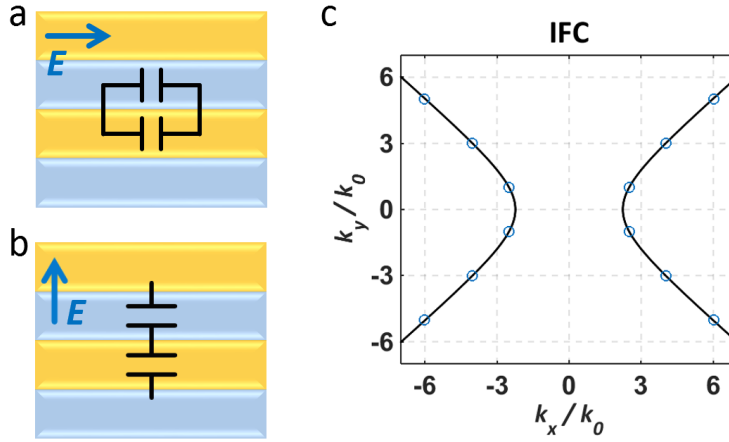


Figure 2.2. (a)-(b) Equivalent capacitor model for (a)  $\epsilon_{\parallel}$  and (b)  $\epsilon_{\perp}$ . (c) IFCs from EMA (solid line) and the Fourier modal method (circle).

Because of their hyperbolic dispersion, HMMs have unique properties for extraordinary waves, allowing various novel applications. Since phase and group velocities in HMMs have opposite signs of tangential components along one or two of the principal axes, negative refraction could occur at interfaces with definite media [18]. HMMs also allow high- $k$  propagating waves which enable imaging below diffraction limits [19], and strong light-matter interactions, such as subwavelength optical resonators [20] and super absorbers [21]. High photonic density of states in HMMs could enhance the Purcell effect, and thus allows tailoring light-emitting properties [22].

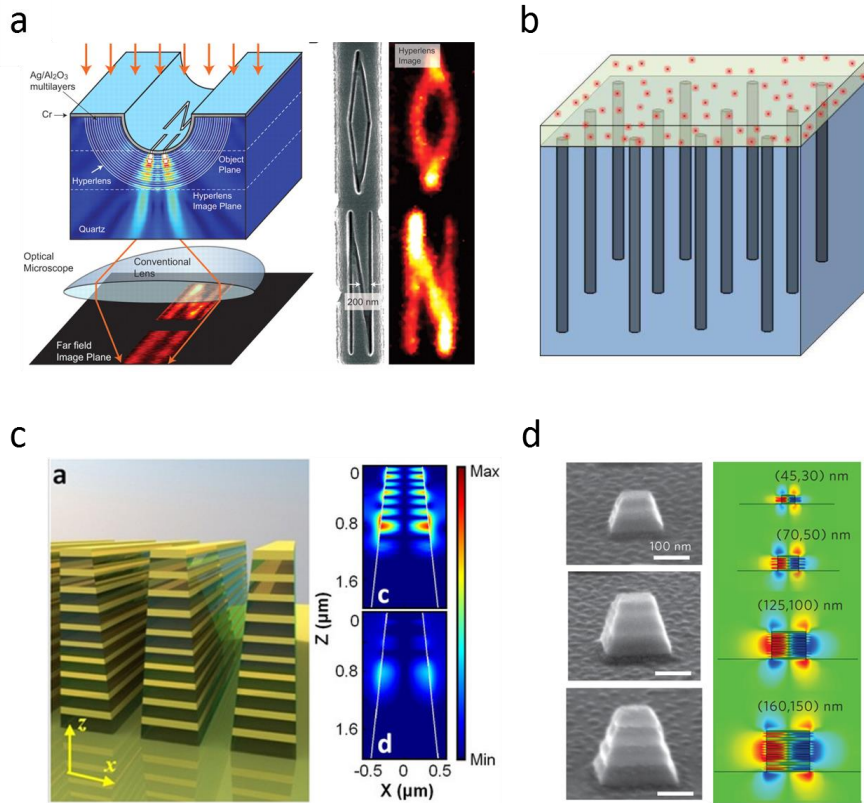


Figure 2.3. Applications of HMMs: (a) hyperlens for imaging below diffraction limit [19], (b) enhanced Purcell effect for quantum dots [22], (c) broadband absorber [21], and (d) subwavelength resonator with anomalous scaling laws [20].

## 2.2 Numerical methods

Because the metal-dielectric layered HMMs have simple structures with one-dimensional periodicity, the Fourier Modal Method (FMM) is appropriate to analyze the modal properties of HMMs. In FMM, the Bloch modes of HMMs are approximately obtained by solving truncated eigenvalue equations in Fourier space,

and thus it is important to decrease the truncation order of Fourier components for efficient calculations. However, because of the Gibbs phenomena, metal-dielectric boundaries require a large number of Fourier components to achieve converged results [23]. Therefore, several methods should be used together with FMM for better convergence conditions.

### 2.2.1 Correct factorization rule

In the macroscopic Maxwell's equations, normal components of displacement fields should be continuous at a boundary between different materials. In contrast, normal electric fields are discontinuous at the boundary because of discontinuous material parameters. In this situation, the convolution of electric fields and material parameters should be correctly factorized to ensure that truncated Fourier series converge at the discontinuous boundary as the truncation order is increased. The correct factorization rule was formulated by Li, called inverse rule (IR) [24]. When continuous  $D_n$  are the product of  $E_n$  and  $\varepsilon_n$  which are simultaneously discontinuous at the boundary, the Fourier components of each functions satisfy the following relations:

$$D_n = \varepsilon_n E_n \quad \Rightarrow \quad [D_n]_i = \left[ \frac{1}{\varepsilon_n} \right]_{ij}^{-1} [E_n]_j \quad (2.6)$$

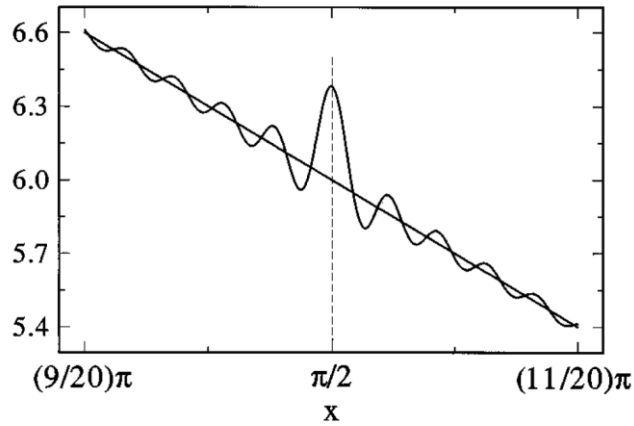


Figure 2.4. Example results of Fourier factorizations based on the Laurent's rule (oscillatory line) and IR (nonoscillatory line) [24].

### 2.2.2 Adaptive spatial resolution

In addition to IR, adaptive spatial resolution (ASR) also provides improvement of convergence conditions by decreasing the material discontinuity [23]. Since it is the boundaries between different materials where a large number of Fourier components are required to reflect their sharp variations of material parameters, the magnitude of the material discontinuity is a significant factor to determine the degree of convergence. Thus, a fast convergence can be achieved by effectively decreasing the material discontinuity using a coordinate transformation. In the coordinate systems which have high spatial resolution near the material discontinuity, the material parameters are multiplied by small components of the metric tensor at the boundary, allowing converged results at a relatively low truncation order.

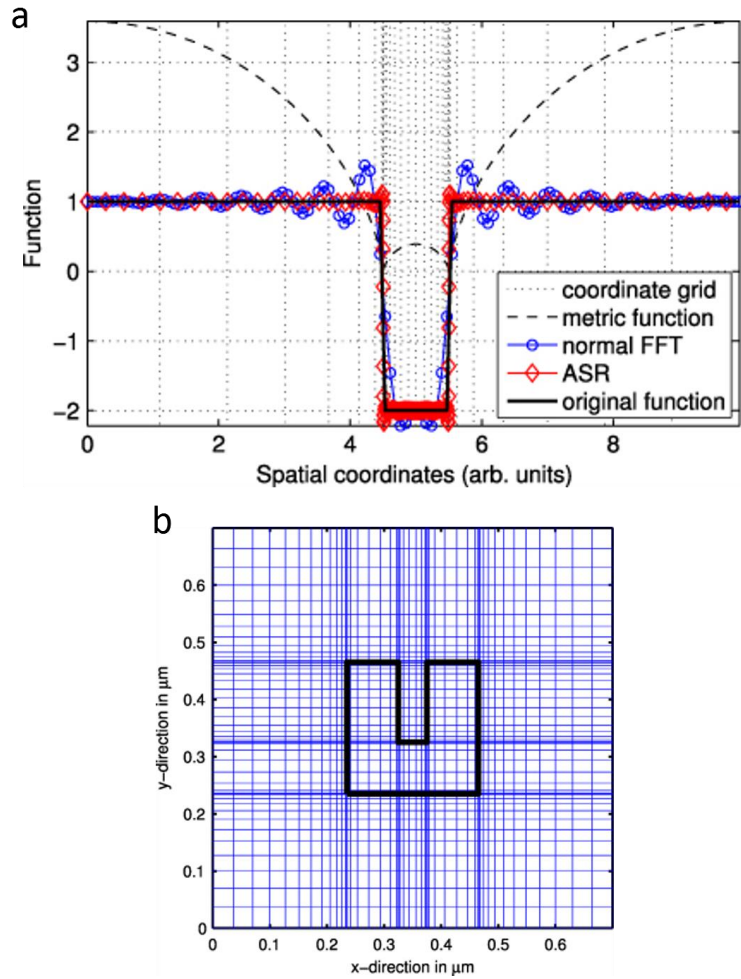


Figure 2.5. Examples of ASR: (a) finite Fourier series in different coordinate systems, and (b) adaptive coordinates for a single split-ring resonator [23].

## 2.3 Fabrication

The metal-dielectric layered HMMs can be easily fabricated through multilayer deposition by virtue of their simple laminar structures. Depending on operating frequency ranges, various materials have been used to create HMMs [17]. In the

range of visible and near-infrared frequency, silver (Ag) and germanium (Ge) can be used as plasmonic and dielectric materials, respectively. Especially, since Ge provide a good wetting effect originating from its high surface energy, alternating deposition of Ag and Ge allows construction of ultra-smoothly multilayered HMMs [20].

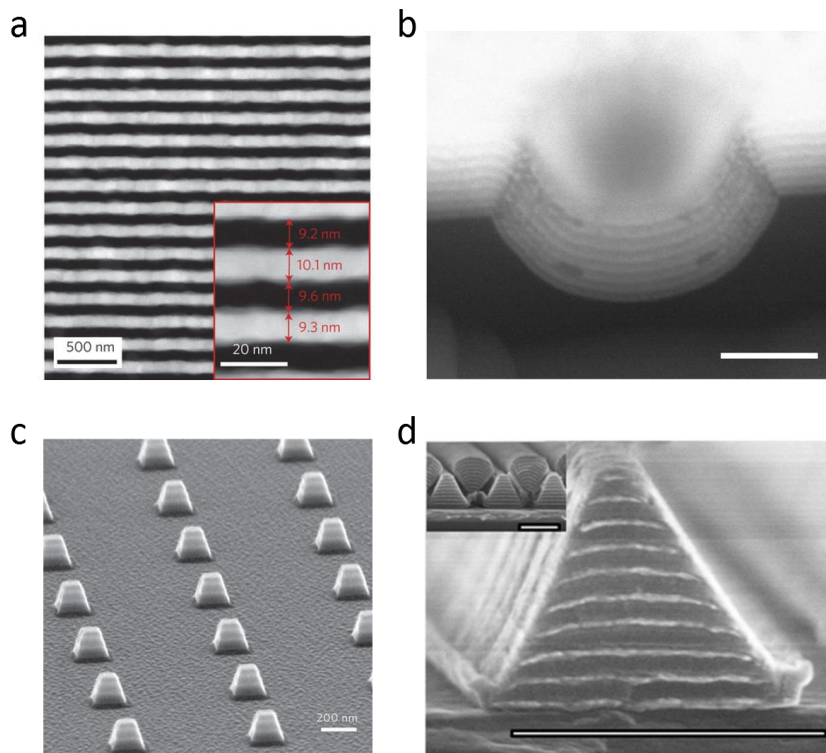


Figure 2.6. Fabrication examples of HMMs: (a) metal-dielectric multilayer [25], (b) spherical hyperlens [26], (c) optical resonator [20], and (d) broadband absorber [27].

For example, we fabricate a one-dimensionally modulated HMM through stepper photolithography, multilayer deposition using E-beam evaporation, and lift-

off process. To define a sub-micron line-and-space pattern, we use the positive photoresist SS03A9 of 850 nm thickness which is spin-coated at 4500 rpm. After defining the one-dimensional pattern in the photoresist using Nikon stepper, E-beam evaporation is used to deposit alternating multilayer of 15 nm Ag and 15 nm Ge with the deposition rate of 0.1 nm/s. Then, the multilayered sample is soaked in acetone with ultrasonication to remove the positive photoresist. With additional deposition of 300 nm Ag layer using E-beam evaporation, we can successfully obtain the final target structure (Fig. 2.7). This sample structure could be used to generate Fano coupling between surface and bulk plasmons in HMMs.

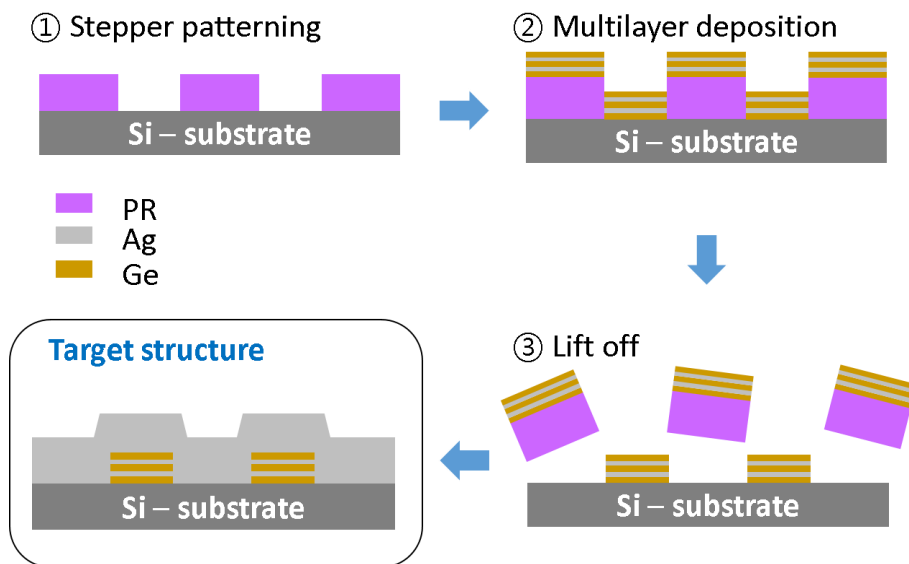


Figure 2.7. Fabrication process of the metal-dielectric layered HMM with one-dimensionally periodic modulation.

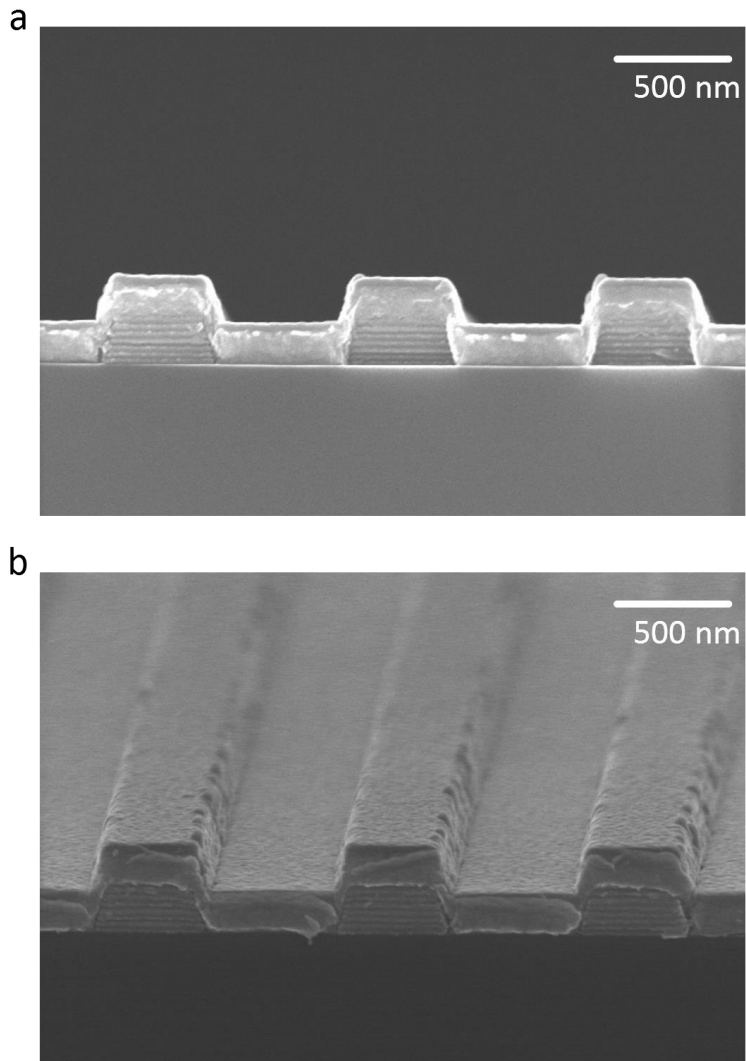


Figure 2.8. SEM images of the fabricated HMM at (a) cross-section view and (b) tilted view.

## Chapter 3

# Interface between HMMs

In this chapter, we investigate an artificial interface between identical metamaterials. Firstly, we derive an analytic model of single-interface scattering between identical media, and find the necessary condition for a zero-thickness metasurface. Based on this analytic analysis, we numerically investigate a dislocated interface in the metal-dielectric layered HMM. As a result, we demonstrate that the dislocated interface allows optical functionalities even with zero-thickness metasurface which provides drastic phase and amplitude discontinuity across a single interface. By exploiting the advantages of ‘zero-thickness’ phase control, we also propose various platforms for applications on controlling wave propagation in HMMs: high- $k$  and low- $k$  mode transitions, and engineering of IFCs.

### 3.1 Boundary conditions for a single interface

We start from boundary conditions for a single interface in two-dimensional media with a permittivity tensor  $\varepsilon=\text{diag}(\varepsilon_x, \varepsilon_y, \varepsilon_z)$  [28]. Under transverse magnetic (TM) incidence ( $E_x, E_y, H_z$ ) on the single interface ( $x=0$ ), transmission ( $t$ ) and reflection ( $r$ ) coefficients for electric fields are given as follows:

$$t = 1 + \frac{1}{2} \left( -i \frac{k_y}{\varepsilon_x} P_x + i \frac{k_x}{\varepsilon_y} P_y \right) \quad (3.1)$$

$$r = \frac{1}{2} \left( i \frac{k_y}{\varepsilon_x} P_x + i \frac{k_x}{\varepsilon_y} P_y \right) \quad (3.2)$$

where  $\mathbf{k}=(k_x, k_y, 0)$  is an incident wavevector, and  $\mathbf{P}=(P_x, P_y, 0)$  is surface electric polarization which is normalized to the incident electric field ( $E_{y,\text{inc}}=1$ ). We only consider non-magnetic materials, so that there is no magnetic polarization on the interface. It is worth noting that the normal and tangential components of  $\mathbf{P}$  are involved in antisymmetric and symmetric scattering of electric fields, respectively, which correspond to magnetic ( $J_{m,z}$ ) and electric ( $J_{e,y}$ ) surface currents.

For the lossless case with a single dipole resonance, the scattering coefficients in Eqs. (3.1) and (3.2) can be expressed as the simple interference forms:

$$t = e^{i\varphi} \cos^2 \left( \theta + \frac{\pi}{4} \right) + \sin^2 \left( \theta + \frac{\pi}{4} \right) \quad (3.3)$$

$$r = \frac{1}{2}(e^{i\varphi} - 1)\cos 2\theta \quad (3.4)$$

where  $\theta = \tan^{-1}(\varepsilon_y k_y P_x / \varepsilon_x k_x P_y)$  for  $-\pi/2 \leq \theta \leq \pi/2$  and  $\varphi = 2\arg(P_x)$  for  $0 \leq \varphi < 2\pi$ .  $\theta$  is defined as the ratio between the electric and magnetic surface currents, roughly corresponding to the incident angle of the wavevector ( $\tan\theta \sim \pm k_y/k_x$ ). Also,  $\varphi$  is the phase derivation of  $\mathbf{P}$  from the incident electric field, and thus corresponds to the degree of mutual coupling between the surface electric dipoles. Figure. 3.1 shows the calculated scattering coefficients based on Eqs. (3.3) and (3.4). The previous studies on metasurfaces have mainly considered the case of  $\theta=0$  where the phase and amplitude of scattering coefficients are strongly coupled to each other. Provided that the normal component of  $\mathbf{P}$  is non-zero ( $P_x \neq 0$ ), however, the single interface can provide drastic transmission phase shift for the oblique incidence ( $\theta \sim \pi/4$ ) while maintaining near-unity transmittance. At the same time, the transmission phase shift can be manipulated by adjusting the coupling intensity of  $\mathbf{P}$  ( $\varphi$ ). Therefore, to obtain the full-range transmission phase shift at a zero-thickness interface, it is required to implement the non-zero normal component of  $\mathbf{P}$  and a strongly coupled system of surface electric dipoles. Because the non-zero normal component of  $\mathbf{P}$  could be naturally induced by breaking the mirror symmetry for the interface, a dislocated interface between identical plasmonic metamaterials is a promising candidate of a zero-thickness metasurface. Thus, we numerically investigate the scattering properties of a dislocated interface in the metal-dielectric layered HMM which is a plasmonic metamaterial with very simple structure.

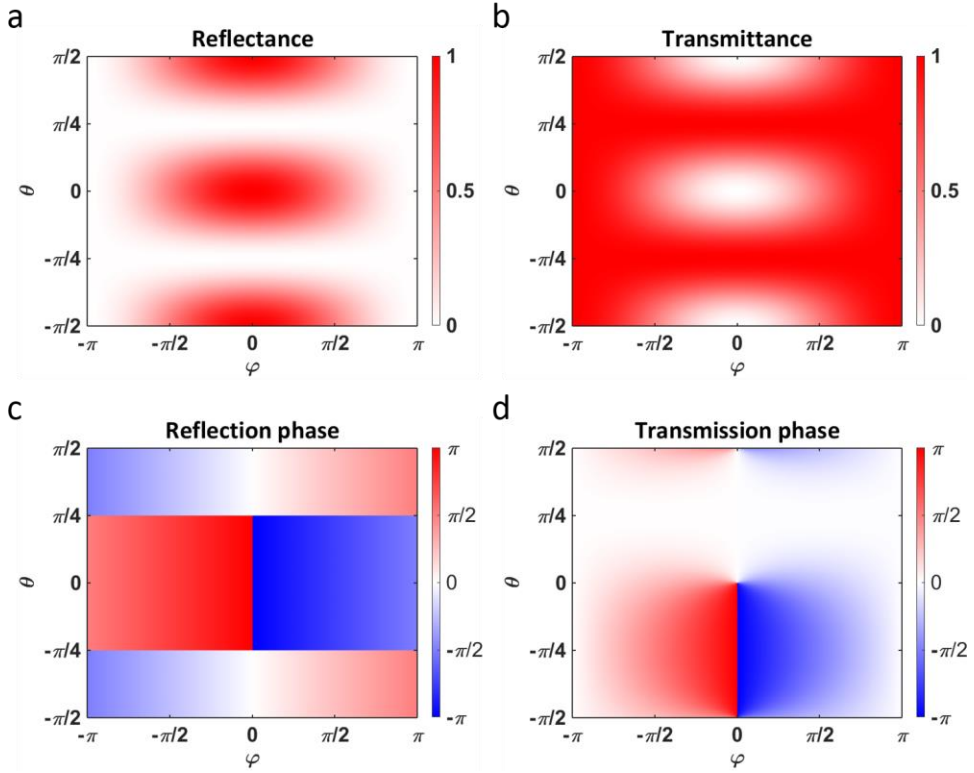


Figure 3.1. According to Eqs. (3.3) and (3.4) for the TM-incidence, (a) reflectance, (b) transmittance, (c) reflection phase and (d) transmission phase as a function of two parameters,  $\theta$  and  $\varphi$ .

### 3.2 Dislocated interface between HMMs

Figure 3.2a shows the schematics of the dislocated HMMs and the metasurface model, which have a  $\Delta$  offset between HMM regions. The scattering properties of the dislocated interface are analyzed numerically by employing the adjusted FMM with IR and ASR for better convergence conditions [23, 24]. To clearly understand the interface physics, we consider the lossless case by neglecting material losses of

the metal and the dielectric. For the thickness of each layer  $d$ , the results of FMM are shown in Fig. 3.3, confirming that the dislocated interface allows optical functionalities even with zero-thickness metasurface. The dislocated interface provides the strong interface scattering even in the deep-subwavelength regime, including singular reflection (Fig. 3.3a) and phase-reversed perfect transmission (Fig. 3.3d). Since the coupling between Bloch modes of HMMs occurs only at the dislocated interface, the resulting scattering can be considered entirely as a single-interface effect.

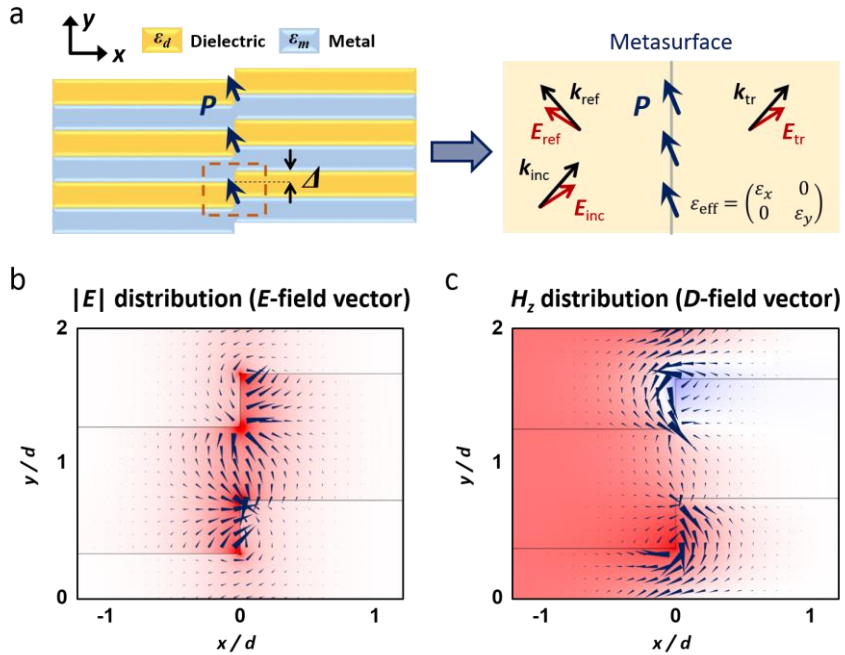


Figure 3.2. (a) Schematics of the dislocated HMMs with dislocation  $\Delta$ , and the metasurface model between identical homogeneous media with an effective permittivity tensor  $\epsilon_{\text{eff}}$ . (b)  $|E|$  distributions and  $E$ -field vectors, and (c)  $H_z$  distributions and  $D$ -field vectors for the singular reflection point ( $d=\lambda/100$ ).

The physics of the dislocated interface can be clearly explained by the analytic metasurface model (Eqs. (3.3) and (3.4)). Comparing Figs. 3.1 and 3.3, the FMM results of the dislocated interface are well-matched to those of the analytic model for the region of  $-\pi/4 \leq \theta \leq \pi/4$ , indicating that the electric surface current plays a dominant role in the scattering of the dislocated interface. For the normal incidence ( $k_y=0$ ), the dislocated interface only supports the electric surface current ( $\theta=0$ ), and thus functions as a perfect electric mirror at the singular reflection point (Fig. 3.3). Note that the dislocation  $\Delta$  corresponds to the parameter  $\varphi$  in Eqs. (3.3) and (3.4), which is related to the mutual coupling between surface electric dipoles. Under the oblique incidence, the transmission phase can be independently controlled by adjusting the structural parameter  $\Delta$ .

For the singular reflection point, the field distributions near the dislocated interface manifest more clearly the origin of the interface scattering. In Fig. 3.2b, the electric field distributions show that local capacitance between adjacent metallic corners provide oblique electric dipole moments at the dislocated interface, which strongly interact with the neighbors through metallic connections. Figure 3.2c also shows the displacement current flow along the dislocated interface, which results from harmonic time variations of the surface electric dipole moments.

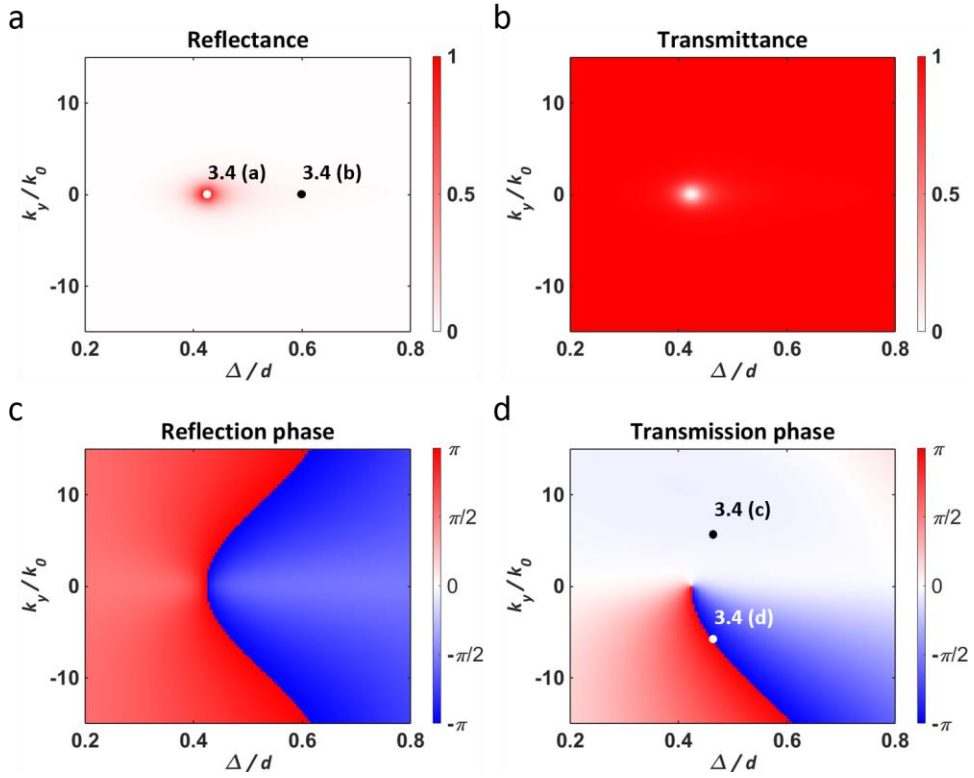


Figure 3.3. (a) Reflectance, (b) transmittance, (c) reflection phase and (e) transmission phase under the fundamental mode incidence from the bulk HMM as a function of dislocation  $\Delta$  and tangential wavevector  $k_y/k_0$  ( $d=\lambda/100$ ).

The displacement currents resulting from the surface electric polarization are also clearly shown in the magnetic field distributions ( $H_z$ ) for singular reflection (Fig. 3.4a) and phase-reversed perfect transmission (Fig. 3.4d). As mentioned earlier, these displacement currents which flow meanderingly along the dislocated interface provide the drastic phase and amplitude discontinuity of magnetic fields across the surface, allowing the strong interface scattering even between the identical effective media.

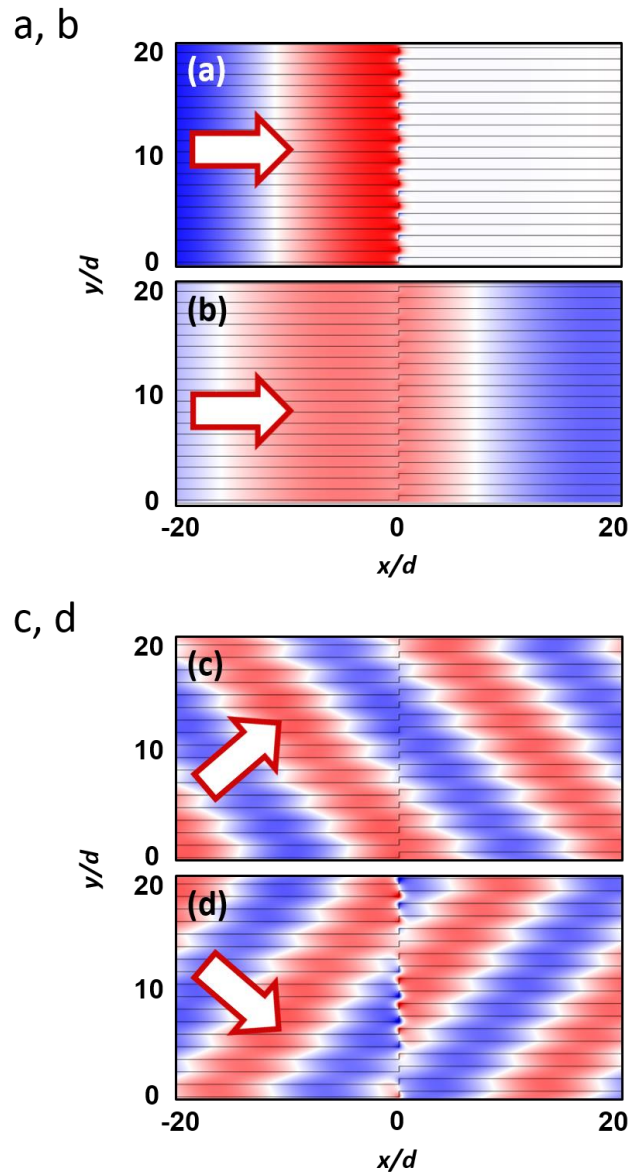


Figure 3.4. Magnetic field distributions ( $H_z$ ) for the specific cases: (a) perfect reflection and (b) perfect transmission for the normal incidence  $k_y/k_0=0$ , and (c) phase-maintained and (d) phase-reversed perfect transmission for the oblique incidences  $k_y/k_0=\pm 5$  ( $d=\lambda/100$ ).

### 3.3 High- $k$ and low- $k$ mode transitions

Exploiting the almost  $2\pi$ -range controllable transmission phase shift with unity transmittance, the dislocated interface can be employed for wavefront manipulation in HMMs. Especially, since HMMs allow high- $k$  propagating waves, we can design the dislocated interface with position-dependent dislocations for high- $k$  and low- $k$  mode transitions.

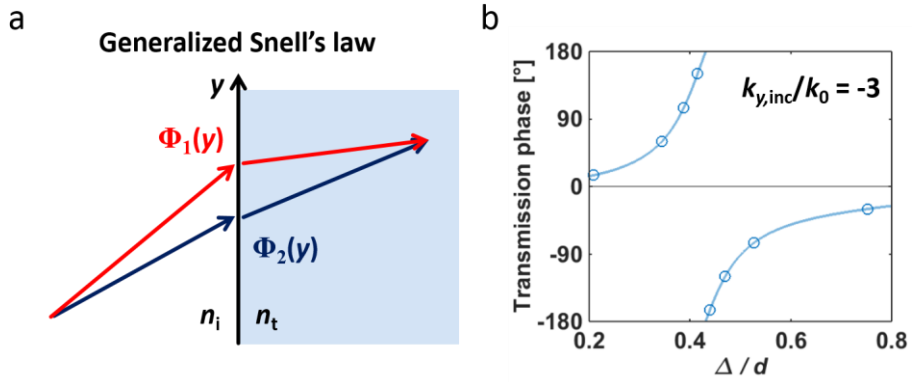


Figure 3.5. (a) Schematic of the generalized Snell's law with a phase gradient [9]. (b) Different values of  $\Delta$  which are chosen for forming a linear phase gradient in steps of  $\pi/8$ .

Insets of Figs. 3.6a and 3.6b show the unit-cell structure for a single transmission phase, which consists of the double 'local' dislocated interface with the identical dislocation  $\Delta$  but opposite directions. One of these local interfaces is introduced to recover the original structure for the incidence without disturbing the transmission phase shift at the position. Note that the single unit cell is composed of three periods of HMMs with the identical dislocation because the scattering

properties of the dislocated interface stem from the coupling effect between each period. Then, to implement the high- $k$  mode transition for the oblique incidence with the tangential wavevector  $k_y/k_0=-3$ , the different values of  $\Delta$  are chosen for the phase shifts ( $\Phi$ ) in steps of  $\pi/8$  (Fig. 3.5b), and arranged monotonically for the constant phase gradient ( $\Delta k_y=d\Phi/dy<0$  for  $k_{y,\text{inc}}<0$ ). In Fig. 3.6a, the magnetic field distribution ( $H_z$ ) shows that the low- $k$  incident wave is converted to the high- $k$  wave as traveling through the designed intermediate structure between the original HMMs. By using the identical values of  $\Delta$  with the reversed arrangement (i.e. the constant phase gradient with opposite sign,  $\Delta k_y=d\Phi/dy>0$  for  $k_{y,\text{inc}}<0$ ), the designed structure can also exhibit the low- $k$  mode transition with anomalous refraction (Fig. 3.6b).

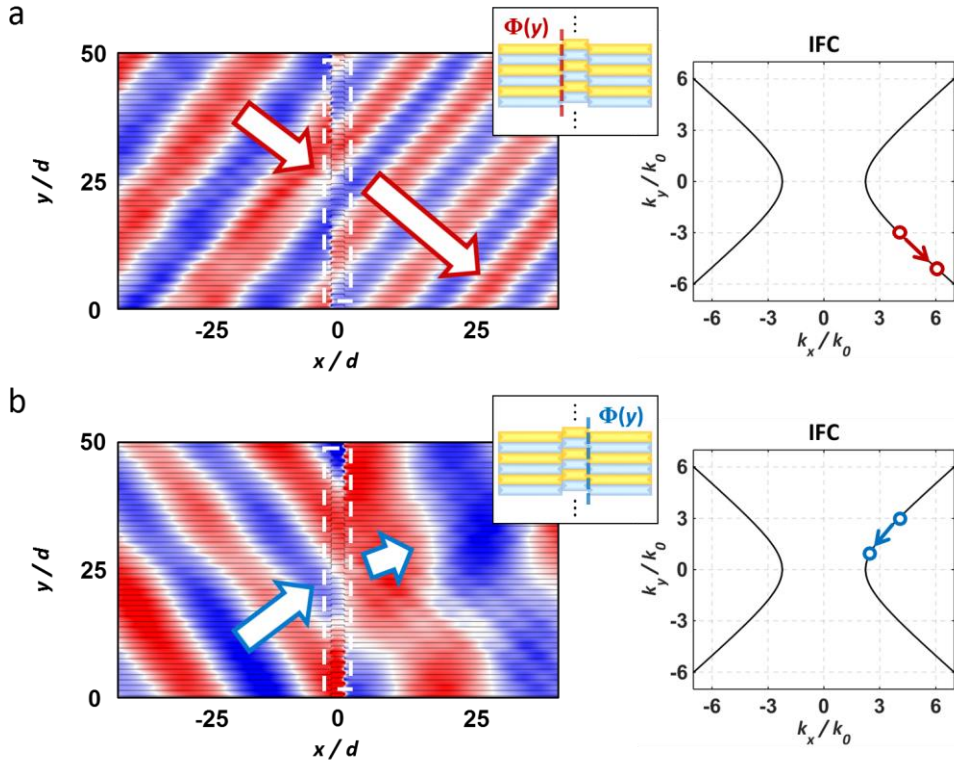


Figure 3.6. The magnetic field distributions ( $H_z$ ) for (a) high- $k$  and (b) low- $k$  mode transitions with the values of  $\Delta$  which are chosen in Fig. 3.5b. Insets in (a) and (b) show the schematics of the unit cell structure for local transmission phase.

### 3.4 Engineering of isofrequency contours

From the sequential scattering at the dislocated interface, we can also manipulate wave propagation through HMMs. In the case that distances between the dislocated interfaces are far enough to neglect near-field coupling between each other, wave propagation through the interface array can be approximately described by using the transfer matrix method (TMM). For the periodic array of alternating dislocated

interfaces with the identical dislocation  $\Delta$  but opposite directions (inset of Fig. 3.7a), the transfer matrix ( $\mathbf{T}$ ) for single-period translation is obtained from the scattering properties of each dislocated interface, allowing the calculation of dispersion relations in  $k$ -space [29].

$$\begin{aligned} T(k_y; \Delta, L_x) = & \frac{1}{t_+} \begin{pmatrix} t_+ t_- - r_+ r_- & r_+ \\ -r_- & 1 \end{pmatrix} \begin{pmatrix} e^{ik_x L_x / 2} & 0 \\ 0 & e^{-ik_x L_x / 2} \end{pmatrix} \\ & \times \frac{1}{t_-} \begin{pmatrix} t_+ t_- - r_+ r_- & r_- \\ -r_+ & 1 \end{pmatrix} \begin{pmatrix} e^{ik_x L_x / 2} & 0 \\ 0 & e^{-ik_x L_x / 2} \end{pmatrix} \end{aligned} \quad (3.5)$$

where  $t_{\pm}=t(\pm k_y; \Delta)$  and  $r_{\pm}=r(\pm k_y; \Delta)$  are the transmission and reflection coefficients for dislocation  $\Delta$ ,  $L_x$  is the period of the dislocated-interface array, and  $k_x$  is a normal wavevector to the dislocated interfaces. Because the transfer matrix is a function of  $\Delta$  and  $L_x$ , wave propagation through HMMs can be manipulated from the structural modulation of the periodic array. In Fig. 3.7a, the calculated IFCs are shown as a function of  $\Delta$  for  $L_x=6d$ . Under the oblique incidence, the dislocated-interface array provides additional normal wavevector by periodical addition of transmission phase at the interfaces (blue lines in Fig. 3.7a). On the other hand, the periodic interface array leads to Bragg reflection and create a band gap for the normal incidence (red lines in Fig. 3.7a). As a result, the IFC of HMM can be greatly modulated by adjusting  $\Delta$ , from the curvature of hyperbolic relations to phase transitions in  $k$ -space.

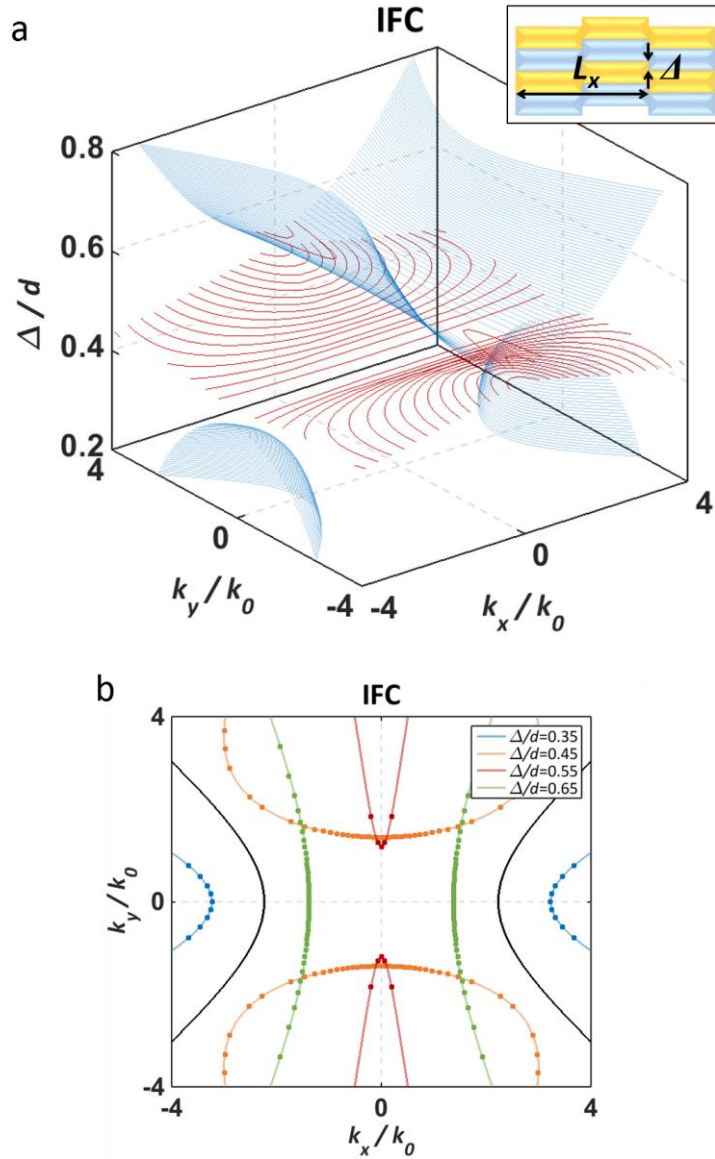


Figure 3.7. The modulated IFCs of HMM (a) as a function of  $\Delta$  and (b) for the specific sizes of the dislocation ( $\Delta/d=0.35, 0.45, 0.55, 0.65$ ). The inset in (a) shows the schematic of the periodic array of alternating dislocated interfaces with dislocation  $\Delta$  and period  $L_x$ . (b) The full-wave numerical analysis based on the finite element method confirms the validity of the results from TMM.

## Chapter 4

### Conclusion

In conclusion, we investigate an artificial interface between identical metamaterials as a zero-thickness metasurface. From both analytic and numerical analysis, we demonstrate that a dislocated interface between identical metal-dielectric layered HMMs allows optical functionalities even with zero-thickness metasurface. By developing the analytic model of single-interface scattering between identical media, we first find the necessary condition for a zero-thickness metasurface. To satisfy this condition, we employ a dislocated interface in plasmonic metamaterials, especially the metal-dielectric layered HMM. From the numerical analysis based on the adjusted FMM with IR and ASR, it is shown that under an oblique incidence, the dislocated interface in HMM provides the full-range transmission phase shift with unity transmittance, which can be manipulated by adjusting the magnitude of dislocation. By exploiting the advantages of tunable phase shift with zero-thickness metasurface, we also propose the platforms for applications on controlling wave

propagation in HMMs: high- $k$  and low- $k$  mode transitions, and engineering of IFCs.

# Bibliography

1. Y. Liu and X. Zhang, "Metamaterials: a new frontier of science and technology," *Chemical Society Reviews* **40**, 2494-2507 (2011).
2. R. A. Shelby, D. R. Smith, and S. Schultz, "Experimental verification of a negative index of refraction," *Science* **292**, 77-79 (2001).
3. M. Choi, S. H. Lee, Y. Kim, S. B. Kang, J. Shin, M. H. Kwak, K. Y. Kang, Y. H. Lee, N. Park, and B. Min, "A terahertz metamaterial with unnaturally high refractive index," *Nature* **470**, 369-373 (2011).
4. M. Silveirinha and N. Engheta, "Tunneling of electromagnetic energy through subwavelength channels and bends using epsilon-near-zero materials," *Physical Review Letters* **97**(2006).
5. J. B. Pendry, D. Schurig, and D. R. Smith, "Controlling electromagnetic fields," *Science* **312**, 1780-1782 (2006).
6. U. Leonhardt, "Optical conformal mapping," *Science* **312**, 1777-1780 (2006).
7. N. Engheta, "Circuits with light at nanoscales: Optical nanocircuits inspired by metamaterials," *Science* **317**, 1698-1702 (2007).
8. D. Schurig, J. J. Mock, B. J. Justice, S. A. Cummer, J. B. Pendry, A. F. Starr, and D. R. Smith, "Metamaterial electromagnetic cloak at microwave frequencies," *Science* **314**, 977-980 (2006).
9. N. F. Yu, P. Genevet, M. A. Kats, F. Aieta, J. P. Tetienne, F. Capasso, and Z. Gaburro, "Light Propagation with Phase Discontinuities: Generalized Laws of Reflection and Refraction," *Science* **334**, 333-337 (2011).
10. S. L. Sun, K. Y. Yang, C. M. Wang, T. K. Juan, W. T. Chen, C. Y. Liao, Q. He, S. Y. Xiao, W. T. Kung, G. Y. Guo, L. Zhou, and D. P. Tsai, "High-Efficiency Broadband Anomalous Reflection by Gradient Meta-Surfaces," *Nano Letters* **12**, 6223-6229 (2012).
11. F. Monticone, N. M. Estakhri, and A. Alu, "Full Control of Nanoscale Optical Transmission with a Composite Metascreen," *Physical Review Letters* **110**(2013).
12. M. A. Kats, R. Blanchard, P. Genevet, and F. Capasso, "Nanometre optical coatings based on strong interference effects in highly absorbing media," *Nature*

Materials **12**, 20-24 (2013).

13. A. H. Abdelrahman, A. Z. Elsherbeni, and F. Yang, "Transmitarray Antenna Design Using Cross-Slot Elements With No Dielectric Substrate," *Antennas and Wireless Propagation Letters, IEEE* **13**, 177-180 (2014).
14. C. Pfeiffer and A. Grbic, "Metamaterial Huygens' Surfaces: Tailoring Wave Fronts with Reflectionless Sheets," *Physical Review Letters* **110**(2013).
15. A. Moreau, C. Ciraci, J. J. Mock, R. T. Hill, Q. Wang, B. J. Wiley, A. Chilkoti, and D. R. Smith, "Controlled-reflectance surfaces with film-coupled colloidal nanoantennas," *Nature* **492**, 86-89 (2012).
16. A. Poddubny, I. Iorsh, P. Belov, and Y. Kivshar, "Hyperbolic metamaterials," *Nature Photonics* **7**, 948-957 (2013).
17. P. Shekhar, J. Atkinson, and Z. Jacob, "Hyperbolic metamaterials: fundamentals and applications," *Nano Convergence* **1**, 1-17 (2014).
18. A. Fang, T. Koschny, and C. M. Soukoulis, "Optical anisotropic metamaterials: Negative refraction and focusing," *Physical Review B* **79**(2009).
19. Z. Liu, H. Lee, Y. Xiong, C. Sun, and X. Zhang, "Far-field optical hyperlens magnifying sub-diffraction-limited objects," *Science* **315**, 1686 (2007).
20. X. D. Yang, J. Yao, J. Rho, X. B. Yin, and X. Zhang, "Experimental realization of three-dimensional indefinite cavities at the nanoscale with anomalous scaling laws," *Nature Photonics* **6**, 450-454 (2012).
21. D. X. Ji, H. M. Song, X. Zeng, H. F. Hu, K. Liu, N. Zhang, and Q. Q. Gan, "Broadband absorption engineering of hyperbolic metafilm patterns," *Scientific reports* **4**(2014).
22. M. A. Noginov, H. Li, Y. A. Barnakov, D. Dryden, G. Nataraj, G. Zhu, C. E. Bonner, M. Mayy, Z. Jacob, and E. E. Narimanov, "Controlling spontaneous emission with metamaterials," *Optics Letters* **35**, 1863-1865 (2010).
23. T. Weiss, N. A. Gippius, S. G. Tikhodeev, G. Granet, and H. Giessen, "Efficient calculation of the optical properties of stacked metamaterials with a Fourier modal method," *Journal of Optics A: Pure and Applied Optics* **11**(2009).
24. L. F. Li, "Use of Fourier series in the analysis of discontinuous periodic structures," *JOSA A* **13**, 1870-1876 (1996).
25. D. Lu, J. J. Kan, E. E. Fullerton, and Z. W. Liu, "Enhancing spontaneous emission rates of molecules using nanopatterned multilayer hyperbolic metamaterials," *Nature Nanotechnology* **9**, 48-53 (2014).
26. J. Rho, Z. L. Ye, Y. Xiong, X. B. Yin, Z. W. Liu, H. Choi, G. Bartal, and X. A. Zhang, "Spherical hyperlens for two-dimensional sub-diffractive imaging at visible frequencies," *Nature Communications* **1**(2010).
27. J. Zhou, A. F. Kaplan, L. Chen, and L. J. Guo, "Experiment and Theory of the Broadband Absorption by a Tapered Hyperbolic Metamaterial Array," *Acs Photonics* **1**, 618-624 (2014).
28. M. Albooyeh, D. Morits, and C. Simovski, "Electromagnetic characterization of substrated metasurfaces," *Metamaterials* **5**, 178-205 (2011).
29. A. Yariv and P. Yeh, *Optical waves in crystals : propagation and control of laser radiation* (Wiley,1984).

# Abstract in Korean

매질 간 계면은 입자 흐름의 불연속을 유발함으로써 근본 입자들의 흐름 제어에 있어 중요한 역할을 해왔다. 광학 분야에서는 계면을 통한 효율적인 파동벡터 변화가 거울과 렌즈, 도파 관 같은 광학 소자들의 기초가 되어왔다.

이와 같은 계면이 서로 다른 매질의 사이에서 구성되어야 한다는 기존 생각을 넘어서, 최근 제안된 ‘메타표면’은 동일한 매질의 내부 혹은 사이에서 형성되면서도 위상과 진폭의 불연속을 통해 강한 파동 산란을 일으킨다. 그러나 제안된 메타표면들은 이러한 산란을 증가시키기 위해 유한한 두께를 가진 요소들로 이루어지면서, 단일 계면의 장점이 충분히 활용되지 못했다.

본 학위 논문에서는 동일한 메타물질 간의 인공적인 계면을 이론 및 수치해석적으로 분석해보았다. 이를 통해, 쌍곡선형 메타물질 간의 단일 단층 계면에서 ‘위상 반전’을 포함한 전 범위의 투과 위상 변화를 얻을 수 있음을 확인하였다. 그리고 이러한 단일 계면의 위상 조절 특성을 활용하여, 쌍곡선형 메타물질 내에서의 파동 흐름 제어를 위한 단층 계면 기반 구조들을 제안해보았다.

**주요어:** 메타표면, 쌍곡선형 메타물질, 단층

**학번:** 2014-21710